Biosensors and Bioelectronics 299 (2026) 118443

Contents lists available at ScienceDirect

Biosensors and Bioelectronics

journal homepage: www.elsevier.com/locate/bios

Dual-strain engineering in Pd metallene for ultrasensitive tetracycline electrochemical biosensing

Yi Wen [a,1], Yinan Dong [b,1], Xuejie Shen [b], Xingyu Luo [b], Ziyi Wang [b], Ruirui Guo [b], Zhituo Geng [b], Peng Li [b], Yongping Huang [b], Xinyu Zhu [a], Jiatong Liu [a], Wangyang Fu [c,*], Zehui Li [b,**], Xiaoyan Zhang [a,***]

[a] School of Pharmaceutical Sciences, Capital Medical University, Beijing, 100069, PR China
[b] State Key Laboratory of Green Papermaking and Resource Recycling, School of Environmental Science and Engineering, Shanghai Jiao Tong University, Shanghai, 200240, PR China
[c] School of Materials Science and Engineering, Tsinghua University, Beijing, 100084, PR China

ARTICLE INFO

Keywords:
Pd metallene
Synergistic doping
Electrocatalytic oxidation
Antibiotic sensing
Biosensing

ABSTRACT

Precise modulation of strain and electronic structure via atomic-level Mo and Cr co-doping in Pd metallene (MoCr-Pdene) significantly enhances electrocatalytic tetracycline (TC) sensing. Conventional Pd-based sensors suffer from weak TC affinity and sluggish kinetics due to surface inertness and biofouling. MoCr-Pdene overcomes these limitations through synergistic dual-strain effects, including compressive strain (from Cr) stabilizing the lattice and tensile strain (from Mo) redistributing surface charge. This strain-charge synergy shortens the Pd-O adsorption distance (1.82 Å), enhances adsorption energy (0.86 eV), and accelerates electron transfer, enabling an ultra-low detection limit of 27 nM, which represents ten-fold improvement over commercial Pd/C. The co-doped metallene exhibits exceptional stability (retaining 80 % of its signal after 120 days) and anti-biofouling capability in matrices. Importantly, MoCr-Pdene serves as a dual-functional platform for clinical diagnostics and environmental monitoring, quantitatively assessing TC biodegradation by black soldier fly larvae (BSFL) and gut microbiota (degradation rates: 97.96 % in frass, 90.67 % in BSFL). These results pioneer atomic-scale strain-electronic engineering for next-generation antibiotic sensing and sustainable bioremediation.

1. Introduction

Tetracycline (TC), a globally prevalent antibiotic with annual consumption exceeding 100,000 tons, poses severe public health and ecological threats. Its accumulation in ecosystems fuels antibiotic resistance, contributing to millions of deaths annually (Heasley, 2011). For instance, residual TC in biofluids (serum of 2–10 μg/mL and urine of 5–50 μg/mL) risks organ damage in 14–20 % of exposed patients (Blake et al., 2025; Chu et al., 2024; Liu et al., 2024b; Wang et al., 2023; Xu et al., 2024). Concurrently, environmental persistence of TC undermines wastewater treatment and necessitates sustainable remediation strategies like black soldier fly larvae (BSFL)-microbe symbiosis (Xu et al., 2025b). However, quantifying TC in complex matrices (e.g., serum, urine, BSFL tissues) remains challenging due to matrix interference and biofouling.

Conventional analytical techniques, such as high-performance liquid chromatography and mass spectrometry, provide high sensitivity and selectivity but are constrained by the need for time-consuming sample preparation and centralized laboratory infrastructure, which limits their application in point-of-care settings (Khaled et al., 2024; Li et al., 2024a). In contrast, electrochemical sensing offers real-time and on-site detection capabilities (Ahmed et al., 2024), but is hindered by surface-specific limitations that compromise sensitivity, selectivity and long-term stability (Cai et al., 2024; Chen et al., 2025; Li et al., 2025). These challenges arise from several interconnected factors: (1) TC has a low molecular affinity toward traditional sensing interfaces due to its large, planar and zwitterionic molecule (Li et al., 2024b). (2) The charge transfer kinetics are suboptimal due to slow electrochemical oxidation,

* Corresponding author.
** Corresponding author.
*** Corresponding author.
E-mail addresses: fwy2018@mail.tsinghua.edu.cn (W. Fu), zehuili@sjtu.edu.cn (Z. Li), xyzhang@ccmu.edu.cn (X. Zhang).
[1] These authors contributed equally to this work.

https://doi.org/10.1016/j.bios.2026.118443
Received 6 December 2025; Received in revised form 12 January 2026; Accepted 23 January 2026
Available online 27 January 2026
0956-5663/© 2026 Elsevier B.V. All rights are reserved, including those for text and data mining, AI training, and similar technologies.

which involves high activation energy barriers (typically greater than 1.5 eV), especially at the C11-OH site (Rong et al., 2024). (3) Non-specific interactions and biofouling occur in complex biological matrices (Li et al., 2023a).

Recent studies have explored diverse sensing materials, including functional carbon nanotubes (Nekoueian et al., 2024), octahedral Cu_2O/Au nanocomposites (Wei et al., 2024), polyaniline@Cu-BTC frameworks (Zhan et al., 2024), and molecularly imprinted polymers based on nano-Al_2O_3/graphene oxide (Zhao and Zhao, 2023). Although some of these platforms exhibit acceptable sensitivity at nM level and broad detection range (from nM-level to μM-level), they often suffer from poor specificity and susceptibility to interferences in real biofluids. Notably, two-dimensional (2D) Pd metallenes (Pdene) have shown promise for TC detection due to their high specific surface area (~150 m^2/g) (Xie et al., 2025), fast charge transport (electron mobility>1.2 cm^2/V/s)(Yang et al., 2024b) and high intrinsic electrocatalytic activity for small organic molecules (e.g. methanol, formic acid (Liu et al., 2023; Qiu et al., 2023)) than commercial Pd/C. However, their performance is still limited by surface instability in biological environments and insufficient specificity toward structurally complex antibiotics such as TC (Wei et al., 2023). Elemental doping strategies have been employed to enhance the surface properties and catalytic activity of Pdene. For example, chromium (Cr) doping introduces compressive lattice strain, which enhances mass activity (~1.36 A/mg) (Zhang et al., 2022), but often causes structural degradation and surface reconstruction, reducing long-term stability (retaining only 26.8 % activity after 10,000 s) (Liu et al., 2024a). Conversely, molybdenum (Mo) doping induces tensile strain, which improve selectivity (>90 %) and Faradaic efficiency (~78.3 %) at moderate potentials (−0.25 V vs. RHE) (Luo et al., 2019), but reduces catalytic activity under more reductive conditions (dropping to ~60 % at −0.45 V) due to weaker surface binding and decreased conductivity (Zhang et al., 2023).

Here, we propose a dual-element coordination strategy to synergistically engineer strain and electronic effects in five-layer Mo/Cr-modified palladium metallene (MoCr-Pdene) that exhibits exceptional performance in TC electrochemical biosensing. By coupling Cr-induced compressive strain with Mo-driven tensile strain, we optimize surface charge distribution and lattice stability, transforming weak TC physisorption into tilted chemisorption. This dual modulation shortens Pd–O adsorption distances (1.82 Å), elevates adsorption energy (0.86 eV), and localizes reactive sites (Δq = 0.90e), achieving record-low detection limits (27 nM) and robust anti-biofouling performance in clinical samples. Beyond diagnostics, MoCr-Pdene enables real-time monitoring of BSFL-mediated TC biodegradation, which is a critical advance toward sustainable antibiotic remediation. This work establishes atomic-scale strain-electronic engineering as a paradigm for multifunctional electrochemical sensing.

2. Results and discussion

2.1. Design of 2D MoCr-Pdene for TC sensing

The Pd surface, although inherently catalytically active, has limited specificity and binding affinity toward certain functional groups present in TC. The integration of Mo and Cr within the Pd atomic layer is carefully orchestrated to optimize both local coordination geometry and charge transfer efficiency. Initial adsorption simulations validate that the computed Pd-O bond length between TC and the MoCr-Pdene surface is minimized to 1.82 Å, significantly shorter than that observed on single-doped or pristine Pd surfaces (Fig. 1a–d). This shortened bond distance, along with a calculated adsorption energy (E_{ad}) of 0.86 eV, suggests the formation of strong chemisorptive interactions. Compared to single-doping configurations, co-introduction of Mo (electron donor) and Cr (electron acceptor) allows for a more balanced and enhanced modulation of the surface electronic environment, which strengthens the Pd-TC binding (Fig. 1e). This synergistic behavior manifests in enhanced local charge accumulation around the Pd atoms surrounding the dopants (Fig. S1), which facilitates specific electron transfer with TC molecules through functional groups (e.g., hydroxyl and amide).

To achieve precise modulation of chemisorptive interactions, a kinetically controlled sequential-doping strategy was designed for the synthesis of MoCr-Pdene. As illustrated in Fig. 1f, Pd nuclei were first formed to establish a stable 2D metallene framework. Subsequently, Cr$(CO)_6$ and Mo$(CO)_6$ were introduced under mild solvothermal conditions, exploiting their distinct decomposition kinetics to guide spatially ordered diffusion into the Pd lattice. This stepwise incorporation prevents phase segregation and preserves the ultrathin lamellar morphology. The differential reactivity of Cr and Mo precursors will enable their atomically dispersed integration into the lattice, resulting in homogeneous co-doping and strain-balanced configurations. Such structural control may be critical for maximizing interfacial reactivity while maintaining electronic coherence across the 2D domain.

2.2. Synthesis and characterization of MoCr-Pdene

The designed MoCr-Pdene was successfully synthesized and

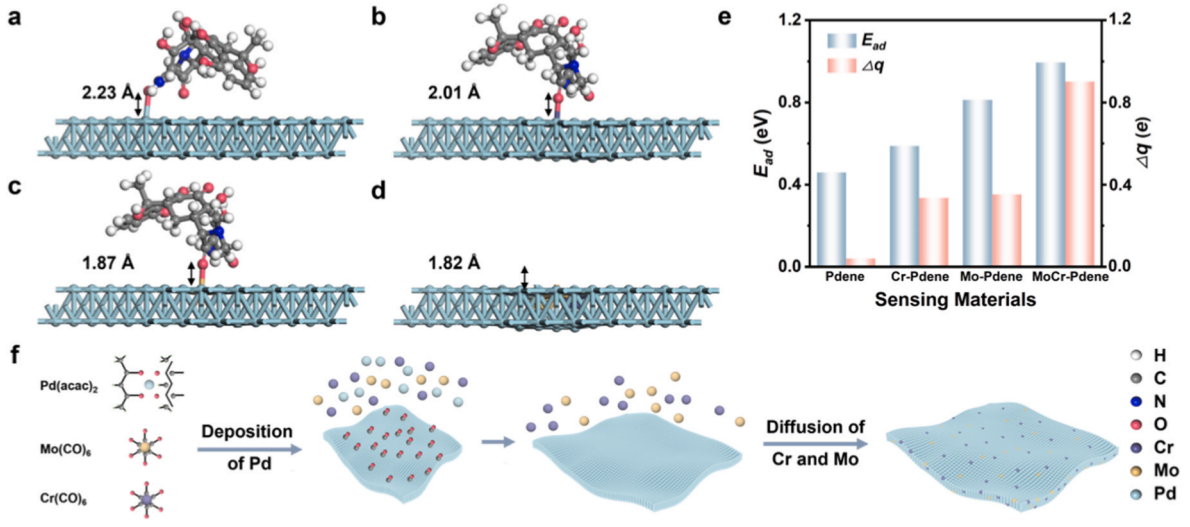


Fig. 1. The absorption configurations of TC on (a) Pdene, (b) Cr-Pdene, (c) Mo-Pdene and (d) MoCr-Pdene. (e) The adsorption energy and charge transfer amount of TC on Pdene, Cr-Pdene, Mo-Pdene and MoCr-Pdene. (f) Scheme of the synthesis process for the 2D MoCr-Pdene.

exhibited a lamellar architecture with uniformly dispersed Pd, Mo, and Cr elements (Fig. 2a). As shown in Fig. 2b, transmission electron microscopy (TEM) image reveals that the synthesized MoCr-Pdene exhibits an ultrathin 2D morphology with folded and wrinkled sheet-like structures and lateral dimensions exceeding to several hundred nanometers. Atomic force microscopy (AFM) image (Fig. 2d) further proves an average thickness of approximately 1.07 nm, equivalent to about five atomic layers (Xie et al., 2024). The formation of 2D MoCr-Pdene is derived from the single-element Pdene nanosheet, which shares a similar structural framework but is obtained with a shorter reaction duration of 0.5 h (Fig. S2). HRTEM analysis further reveals lattice fringe spacing of 0.236 nm in MoCr-Pdene (inset of Fig. 2b), which is slightly smaller than that of pristine Pdene (0.238 nm, inset of Fig. S2). Combining the homogeneous distribution of Pd, Cr, and Mo elements in energy dispersive spectroscopy (EDS) elemental maps (Fig. 2c), Mo and Cr atoms are confirmed to be successfully doped into Pdene lattice with relatively smaller radii (Prabhu et al., 2024). Quantitative analysis by inductively coupled plasma optical emission spectrometry (ICP-OES) reveals that the Mo and Cr contents are 2.39 % and 2.52 %, respectively, with a consistent 1:1 Mo:Cr molar ratio observed even under varying reaction times or precursor ratios (Fig. S3).

The crystal structures of MoCr-Pdene and its derivatives were systematically investigated using powder X-ray diffraction (PXRD). As shown in Fig. 2e, all diffraction patterns of MoCr-Pdene, Mo-Pdene, Cr-Pdene, and Pdene show peaks around 40°, 46°, and 68°, corresponding to the (111), (200), and (220) planes of face-centered cubic (fcc) Pd (JCPDS No. 87–0639) (Song et al., 2024). Compared with pristine Pdene, the diffraction peaks of the others show discernible shifts, indicating dopant-induced lattice strain (Liu et al. 2025a, 2025b). Specifically, Cr doping leads to a shift toward higher 2θ angles, suggesting lattice contraction due to the substitution of Pd atoms by smaller-radius Cr atoms (Ma et al., 2025), whereas Mo doping induces a slight shift toward lower 2θ angles, corresponding to tensile lattice strain (Zhao et al., 2023).

To further elucidate the electronic structure modulation induced by Mo and Cr doping, X-ray photoelectron spectroscopy (XPS) analysis was conducted. As shown in Fig. 2f, the Pd 3d binding energies are notably shifted in the doped systems compared to Pd/C, which reveals peaks at 336.61 eV and 341.93 eV, indicating a relatively free metallic, low-oxidation state Pd (Liu et al., 2023). In Mo-Pdene, the peak shift to 336.13 eV and 341.48 eV, indicating an increase in the electron density on the Pd surface, likely due to electron donation from Mo (Si et al., 2024). For Cr-Pdene, the peaks shift to 336.27 eV and 341.65 eV, suggesting that Cr doping also affects the electronic structure, although the electron transfer mechanism differs from that of Mo (Li et al., 2023b). In MoCr-Pdene, the Pd 3d binding energies (336.20 eV and 341.58 eV) represent a compromise between the two doping elements, suggesting that Mo and Cr synergistically modulate the electronic environment of Pd (Wang et al., 2025a). This optimized electron density on the surface likely enhances the catalytic activity and surface reactivity of Pd in MoCr-Pdene.

2.3. Electrochemical performance of MoCr-Pdene towards TC

To evaluate the electrochemical sensing performance of various catalysts to TC, linear sweep voltammetry (LSV) was employed. As depicted in Fig. 3a, the MoCr-Pdene/C modified glassy carbon electrode (GCE) as sensor exhibits a negligible current response in the absence of TC, while a distinct anodic peak appears at 0.708 V with the addition of 60 μM TC, indicating its electrocatalytic activity toward TC oxidation (Yang et al., 2024a). In comparison, commercial Pd/C, Pdene/C, Cr-Pdene/C, and Mo-Pdene/C sensors show oxidation peaks at 0.689 V, 0.693 V, 0.696 V, and 0.701 V, respectively (Fig. 3b), with gradually improved current responses. The highest current response of MoCr-Pdene/C sensor highlights the synergistic enhancement of co-doping with Mo and Cr atoms, which enhances the catalytic efficiency for TC oxidation (Guo et al., 2023).

To quantify the sensing performance of MoCr-Pdene/C sensor, current-time (i-t) tests were performed at the optimal oxidation potential of 0.708 V (Fig. 2c). The oxidation response current increases gradually with successive additions of TC in the concentration range of 1–60 μM. At 60 μM TC concentration, the current response of the MoCr-Pdene/C sensor is approximately 4-fold higher than that of the commercial Pd/C sensor. Furthermore, as shown in Fig. 3d and summarized in Table S1, MoCr-Pdene/C sensor exhibits well-defined linear calibration curves for TC in the 1–6 μM and 6–60 μM concentration ranges, with rapid response times of 3–5 s. The corresponding linear equations are determined as $y = 0.31x - 0.11$ ($R^2 = 0.996$) and $y = 0.096x + 1.27$

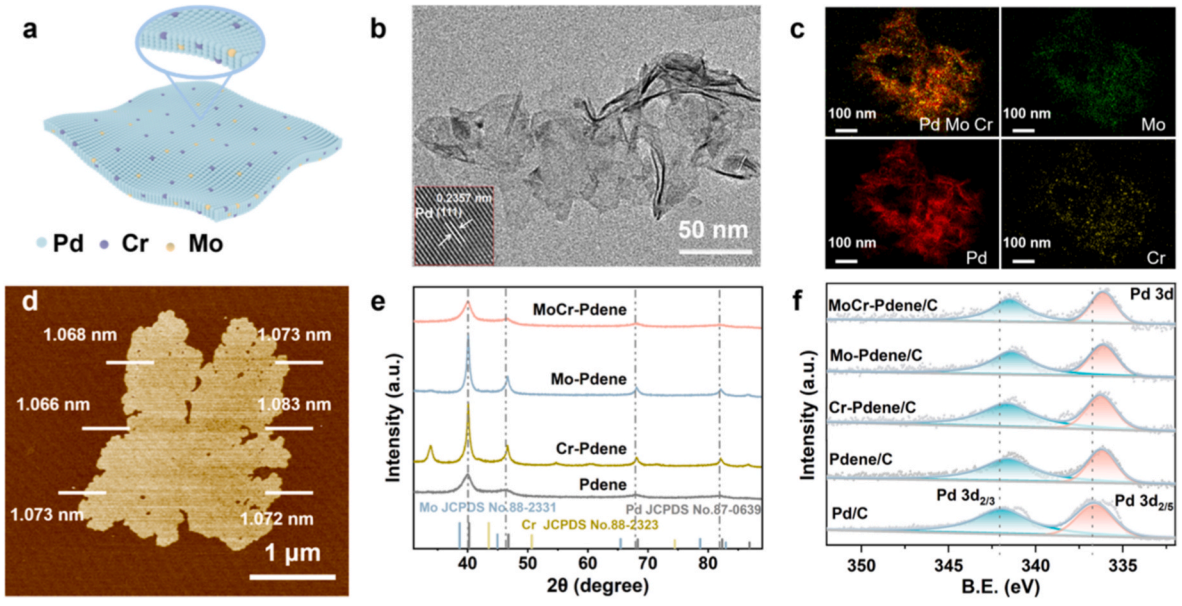


Fig. 2. Morphological and structural characterization of MoCr-Pdene. (a) Schematic illustration of MoCr-Pdene model with five atomic layers of Pd. (b) TEM images (inset is representative lattice spacing), (c) EDS elemental maps, and (d) AFM image of MoCr-Pdene. (e) PXRD patterns of MoCr-Pdene, Mo-Pdene, Cr-Pdene, and Pdene. (f) XPS analysis of MoCr-Pdene/C, Mo-Pdene/C, Cr-Pdene/C, Pdene/C, and Pd/C.

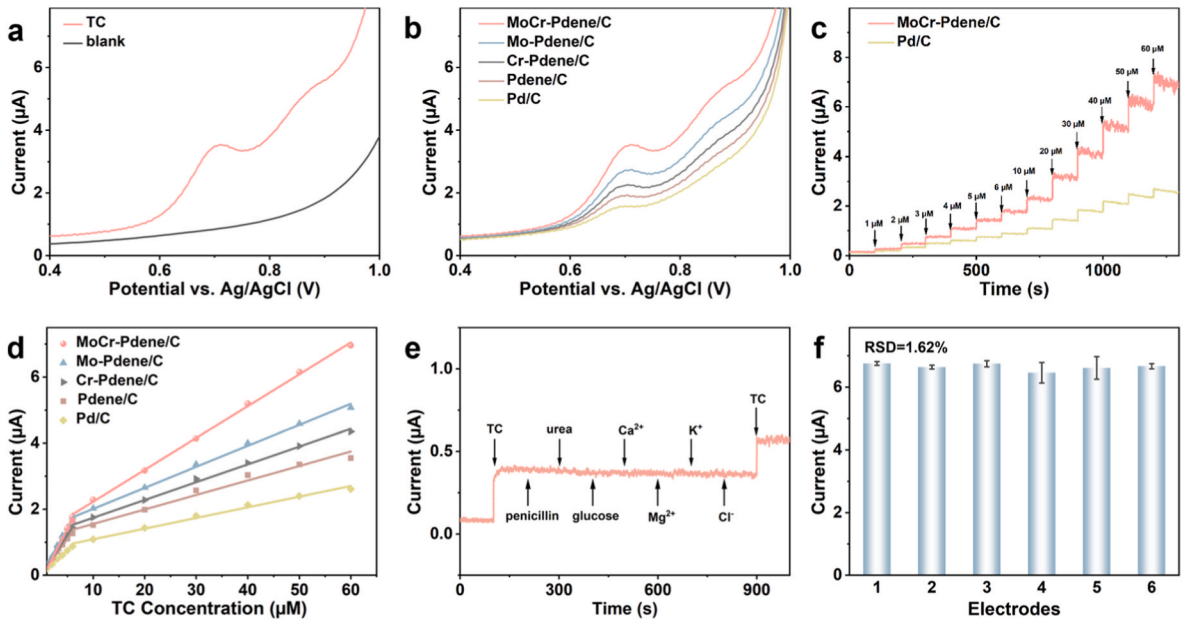


Fig. 3. Electrochemical performance of MoCr-Pdene/C towards TC detection. (a) LSV curves of MoCr-Pdene/C in PBS solution at 60 μM TC concentration. (b) Comparison of oxidation peak currents of MoCr-Pdene/C, Mo-Pdene/C, Cr-Pdene/C, Pdene/C, and Pd/C in the presence of 60 μM TC. (c) i-t response of MoCr-Pdene/C and Pd/C for TC oxidation in the 1–60 μM concentration range. (d) Linear relationship between peak current and TC concentration for MoCr-Pdene/C. (e) i-t responses for interference testing by common species at 1 μM TC. (f) Reproducibility test of MoCr-Pdene/C sensor for TC detection (n = 6).

(R^2 = 0.999), indicating high detection sensitivity across broad concentration range. The limit of detection is calculated based on the standard 3σ/slope method, where σ represents the standard deviation of the blank signal and the slope is obtained from the linear calibration curve (Momeni et al., 2024; Sun et al., 2025; Xu et al., 2025a). In comparison, Pdene/C, Mo-Pdene/C, Cr-Pdene/C, and commercial Pd/C sensors exhibit lower current responses and poor sensitivity, with corresponding detection limits of 267 nM, 127 nM, 129 nM and 272 nM, respectively. The detection limit of MoCr-Pdene/C sensor is calculated to be as low as 27 nM, which represents a significant improvement over other counterparts and also outperforms most existing analytical methods for TC detection (Table S2).

The MoCr-Pdene/C sensor also exhibits good selectivity, durability and repeatability toward TC. As shown in Fig. 3e, it generates a distinct current response to 1 μM TC, while exhibiting negligible responses interference from common interfering species (50 μM), including penicillin, urea, glucose, Ca^{2+}, Mg^{2+}, K^+, and Cl^-. The TC detection signal remains stable after the introduction of interferents, confirming the strong anti-interference capability of the sensing system. The long-term stability of the MoCr-Pdene/C sensor was further evaluated by monitoring the electrochemical response at 15-day intervals over a total storage period of 120 days (Fig. S4). The current response toward 60 μM TC remained above 80 % of its initial value after 120 days, indicating good long-term storage stability. In addition, six MoCr-Pdene/C sensors exhibit a relative standard deviation (RSD) of merely 1.62 % in response to 60 μM TC (Fig. 3f), demonstrating high fabrication reproducibility (Naikoo et al., 2023).

2.4. TC sensing mechanism of MoCr-Pdene

The sensing mechanism of MoCr-Pdene/C toward tetracycline (TC) was investigated through combined electrochemical analyses and density functional theory (DFT) calculations. The electrooxidation of TC on MoCr-Pdene/C proceeds through a diffusion-controlled process involving multiple electron-transfer steps. As shown in Fig. S5b, Cyclic voltammetry (CV) at varying scan rates (20–200 mV/s) exhibits two well-defined anodic peaks, indicating a sequential two-step oxidation process. With increasing scan rate, the anodic peak current (Ip) exhibits a linear relationship with the square root of the scan rate ($\nu^{1/2}$, Fig. S5c, R^2 = 0.999) (Xu et al., 2022), consistent with a diffusion-controlled process governed by the Randles-Ševčík equation (Guo et al., 2019). The number of electrons involved in the TC oxidation process was estimated to be approximately two, consistent with previously reported electrochemical oxidation mechanisms of TC (Guo et al., 2019; Wang et al., 2021a).

To further clarify the involvement of protons, the pH-dependent electrochemical behavior was investigated in 0.1 M PBS with pH values ranging from 3.0 to 7.0 (Fig. S5d). Both anodic peak potentials shift negatively with increasing pH, and the highest oxidation current is observed at pH 3.0, indicating that proton availability plays a crucial role in the reaction kinetics. The linear dependence of peak potential on pH yields slopes of 63 mV/pH and 51 mV/pH for the first and second oxidation steps, respectively, which are close to the theoretical Nernstian value of 59 mV/pH for a $2H^+/2e^-$ process (Xu et al., 2022). This provides strong evidence that TC oxidation on MoCr-Pdene/C follows a proton-coupled electron transfer (PCET) mechanism (Hammes-Schiffer, 2023).

The superior activity of MoCr-Pdene/C is closely linked to its large electrochemically active surface area (ECSA). Using $[Fe(CN)_6]^{3-/4-}$ as a redox probe (Fig. S5a), the redox peak currents exhibit a linear dependence on the square root of the scan rate, confirming a diffusion-controlled process (Guo et al., 2019). Based on the Randles-Ševčík equation, the ECSA of MoCr-Pdene/C was calculated to be 0.73 cm^2, which is significantly higher than those of Mo-Pdene/C (0.63 cm^2), Cr-Pdene/C (0.59 cm^2), Pdene/C (0.34 cm^2), and commercial Pd/C (0.15 cm^2) under same conditions (Fig. S6). This enhancement can be attributed to the strain compensation effect induced by Mo and Cr co-doping. Quantitative refinement of PXRD data reveals lattice constants of 0.3868 nm for pristine Pdene, 0.3864 nm for Cr-Pdene (ca. −0.10 % compressive strain), and 0.3866 nm for Mo-Pdene (ca. −0.05 % strain). In contrast, MoCr-Pdene exhibits a lattice constant of 0.3870 nm, corresponding to a slight tensile strain of ca. +0.05 %. The intermediate lattice constant and diffraction peak position of MoCr-Pdene indicate effective compensation of the opposing lattice distortions introduced by Mo and Cr, which suppresses metal aggregation and preserves a highly accessible electrochemical surface area, thereby facilitating fast charge

transport during TC oxidation.

Based on the electrochemical data and prior literature, a plausible TC oxidation pathway is proposed (Fig. 4a). At lower oxidation potentials, the initial step likely involves the oxidation of the phenolic hydroxyl group at the C10 position, involving the loss of one electron and one proton to form an unstable radical intermediate (Dang et al., 2004). This intermediate subsequently experiences a second deprotonation and electron transfer, yielding a quinone-like intermediate. At higher oxidation potentials, further electrochemical transformation of the intermediate occurs. In acidic media, strong intramolecular hydrogen bonding initially stabilizes the oxidized species. With increasing potential, steric hindrance around the hydroxyl groups at the C7 and C10 positions is reduced, weakening the hydrogen bonds and enabling the sequential release of additional protons (Liang et al., 2018). This process ultimately leads to the formation of a more stable, highly oxidized quinone-like structure.

DFT calculations were employed to rationalize the enhanced performance at the atomic level. The calculated adsorption energies (E_{ad}) of TC on Pdene, Cr-Pdene, Mo-Pdene, and MoCr-Pdene are 0.65, 0.71, 0.77, and 0.86 eV, respectively, with corresponding Pd–O adsorption distances of 2.23, 2.01, 1.87, and 1.82 Å. The higher adsorption energy and shorter Pd–O adsorption distance on MoCr-Pdene indicate a stronger TC-surface interaction. Bader charge analysis reveals significant charge transfer from Mo and Cr to neighboring Pd atoms, with charge transfers of 0.33*e* for Cr-Pdene, 0.35*e* for Mo-Pdene, and 0.90*e* for MoCr-Pdene. This charge redistribution creates local electronic hotspots that strengthen TC binding and facilitate subsequent oxidation steps (Xuan et al., 2023). The free energy profiles for TC oxidation demonstrates that adsorption is thermodynamically favorable on MoCr-Pdene (−0.44 eV) compared to pristine Pdene (0.06 eV), and the energy barrier for the rate-determining step is significantly lowered (Fig. 4b). The subsequent oxidation of TC to TC*** releases more energy on MoCr-Pdene (7.04 eV) than on pristine Pdene (6.98 eV). The rate-determining step (TC*** → TC****) exhibits a significantly lower energy barrier on MoCr-Pdene compared to Pdene. Furthermore, geometrical optimization reveals the formation of Pd-O and Mo-O bonds at the TC-MoCr-Pdene interface, enhancing interfacial anchoring. Charge density difference analysis confirms electron enrichment at the Mo/Cr-Pd interface, which promotes interfacial electron transfer. Collectively, the synergistic co-doping of Mo and Cr optimizes the electronic structure and reaction energetics of Pdene, leading to its superior electrocatalytic activity for TC sensing.

2.5. Application of MoCr-Pdene/C sensor for determining TC

To validate the real-world utility of the MoCr-Pdene/C sensor, a flexible MoCr-Pdene/C sensing platform was fabricated via commercial screen-printing technology for point-of-care deployment in clinical and environmental monitoring (Fig. 5a). (Wu et al., 2023) The sensor exhibits a broad dynamic range (1 μM–2 mM) and ultralow detection limit (27 nM) in PBS containing TC ($y = 0.01633x + 2.41565$, $R^2 = 0.99$, Fig. 5b). Crucially, in spiked human serum and urine, the average recovery rates across the platform are between 93.05 % and 104.94 %, with RSD below 6.19 % (Fig. 5b and Table S3), demonstrating the high reliability and accuracy of the sensor against complex biological matrices (Wang et al., 2025b).

Expanding into environmental biotechnology, we pioneered the use of MoCr-Pdene sensor for real-time monitoring of TC biodegradation in a closed-loop BSFL bioremediation system (Fig. 5a). After 12-day treatment of TC-contaminated waste with BSFL (100 mg/kg), MoCr-Pdene sensor reveals degradation efficiencies of 90.67 % in BSFL and 97.96 % in frass, surpassing conventional biological methods (Fig. 5c and d). To distinguish biological degradation from abiotic effects, a control experiment was conducted using TC-contaminated substrates under identical conditions but without the presence of BSFL. The abiotic control exhibits negligible TC removal (<4.31 %) over the same incubation period, confirming that the observed TC degradation is predominantly driven by BSFL-mediated biological processes (Fig. S7). Mechanistic analysis of *S. marcescens* BSFL-6 gut microbiota identified key enzymatic drivers, which are upregulated tet34 (TC monooxygenase-like enzyme) and UGT2B7 (UDP-glucuronosyltransferase homolog) catalyze oxidative decarboxylation and glucuronidation, converting TC into low-toxicity polar metabolites (P430 and P652). Electrochemical quantification confirmed minimal residue accumulation, verifying the consistency between biochemical and electroanalytical outcomes. Importantly, the MoCr-Pdene electrode exhibits strong anti-fouling behavior even in complex organic matrices, enabling residue detection in protein/lipid-rich larval tissues and establishing electrochemistry-metagenomics synergy for mechanistic validation of bioremediation efficacy.

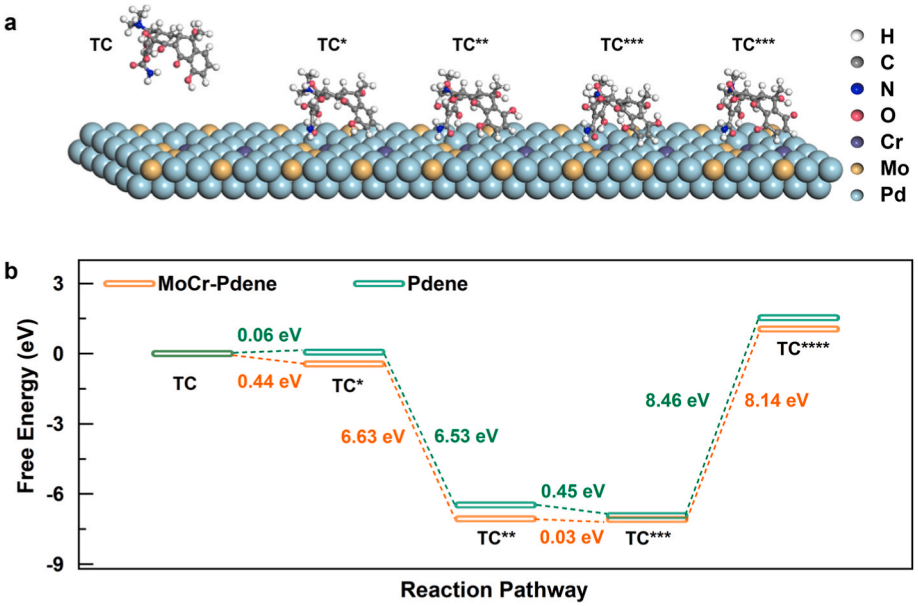


Fig. 4. Mechanism of TC oxidation on MoCr-Pdene/C. (a) Proposed oxidation pathway of TC. (b) DFT-calculated free energy profiles and schematic illustrations on the MoCr-Pdene and pura Pdene surfaces.

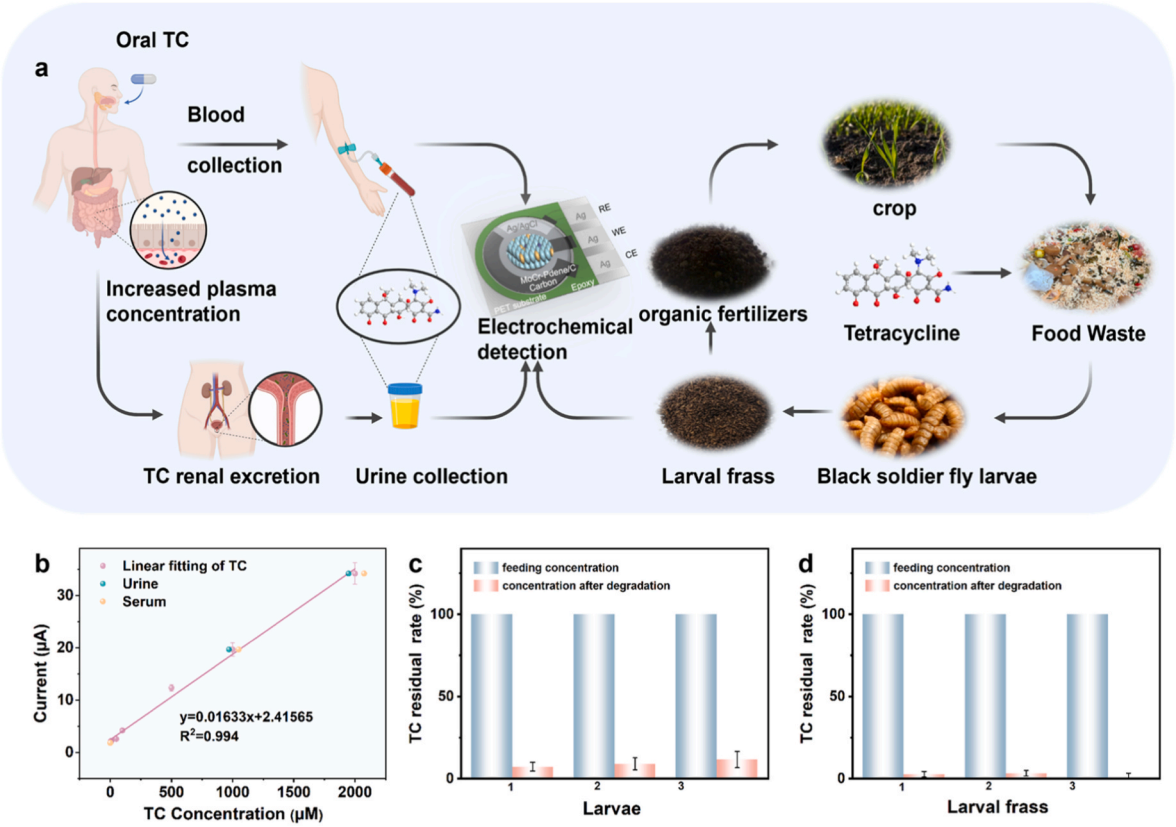


Fig. 5. Validation of MoCr-Pdene/C sensing platform in real-world biological samples. (a) Schematic diagram of TC detection in serum/urine and residual monitoring during BSFL degradation using a screen-printed MoCr-Pdene/C sensor. (b) The linearrelationship of peak current and TC concentration. Degradation rate of TC in BSFL (c) and larval frass (d).

3. Conclusion

In conclusion, we developed a MoCr-Pdene through atomic-scale dual-strain engineering, creating a transformative platform for TC detection and bioremediation monitoring. The synergistic interplay of Cr-induced compressive strain and Mo-driven tensile strain optimizes charge distribution (Δq = 0.90*e*), shortens Pd–O adsorption distance (1.82 Å), and enhances adsorption energy (0.86 eV). This promotes efficient TC oxidation with a broad linear range (1 μM-2 mM) and an ultra-low detection limit of 27 nM. The screen-printed MoCr-Pdene sensor also achieves accurate TC quantification in biofluids (recovery of 93.05–104.94 %) and complex biotransformation matrices, demonstrating degradation efficiencies of 90.67 % in BSFL and 97.96 % in frass via its anti-fouling capability. The sensor design further enables scalable deployment in wearable diagnostics and field monitoring. Our dual-strain engineering strategy establishes a general paradigm for tailoring 2D materials' interfacial properties, bridging precision antibiotic sensing and sustainable bioremediation, which is a critical advance toward One Health solutions.

4. Materials and methods

4.1. Synthesis of MoCr-Pdene, Mo-Pdene, Cr-Pdene and Pdene

MoCr-Pdene was synthesized via a kinetically controlled sequential-doping solvothermal strategy. In a typical procedure, $Cr(CO)_6$ (10 mg), $Mo(CO)_6$ (10 mg), and ascorbic acid (20 mg) were first dissolved in 5 mL of oleylamine under continuous stirring at 70 °C to form a homogeneous precursor solution. After cooling to room temperature, Pd $(acac)_2$ (10 mg) was added, followed by ultrasonication for 10 min to ensure complete dissolution.

The resulting solution was transferred into a sealed reaction vessel and heated at 80 °C for 12 h. During the solvothermal process, the distinct decomposition kinetics of $Cr(CO)_6$ and $Mo(CO)_6$ enable temporally separated incorporation of dopants into the Pd lattice. Specifically, $Cr(CO)_6$ decomposes preferentially at an earlier stage of the reaction, leading to initial Cr incorporation into the forming Pd metallene framework, whereas $Mo(CO)_6$ decomposes more gradually and is incorporated at a later stage. This sequential dopant incorporation effectively suppresses phase segregation and promotes homogeneous co-doping within the ultrathin Pd metallene.

After completion of the reaction, the product was collected by centrifugation, washed three times with cyclohexane to remove residual organic species, and finally redispersed in cyclohexane for subsequent characterization and electrode fabrication.

4.2. Synthesis of MoCr-Pdene/C, Mo-Pdene/C, Cr-Pdene/C and Pdene/C

First, a certain amount of Ketjen black was dispersed in anhydrous ethanol and ultrasonicated for 1 h. Cyclohexane was then added, followed by an additional 0.5 h of ultrasonication to obtain a homogeneous mixture. Subsequently, the metallene material dispersed in cyclohexane was gradually added to the previously prepared mixture and ultrasonicated for another 2 h. Finally, the product was collected by centrifugation and dried overnight at 60 °C, yielding MoCr-Pdene/C, Mo-Pdene/C, Cr-Pdene/C, and Pdene/C.

4.3. Characterization

The PXRD analysis was carried out using a Rigaku D/max-2500/PC diffractometer under operating conditions of 40 kV voltage and 15 mA current, utilizing Cu Kα radiation (λ = 1.5406 Å). The morphological

characteristics were examined via TEM (JEM-2100F microscope). Elemental distribution was mapped using a FEI Talos F200X at an acceleration voltage of 200 kV. AFM imaging was conducted with a Bruker Dimension Icon. The XPS spectra were obtained using an ESCALAB 250Xi spectrometer equipped with an Al Kα cathode source (75–150 W) under ultrahigh vacuum conditions. Elemental composition analysis was performed by inductively coupled plasma optical emission spectrometer (ICP-OES) (Agilent 5110). For PXRD and XPS characterization, MoCr-Pdene/C, Mo-Pdene/C, Cr-Pdene/C, and Pdene/C were supported on commercially available carbon black.

4.4. Electrochemical measurements

A conventional three-electrode configuration was employed for electrochemical measurements. The reference electrode was an Ag/AgCl electrode, while a Pt foil (1 cm × 1 cm) acted as the counter electrode. The working electrode consisted of a GCE (diameter: 4 mm) modified with the catalyst. To prepare the catalyst ink, 1 mg of catalyst was dispersed in a mixture of 500 μL isopropanol, 480 μL ultrapure water, and 20 μL Nafion solution, followed by ultrasonication for 1 h. Afterward, 5 μL of the resulting dispersion was drop-cast onto the GCE surface and dried under ambient conditions to complete the electrode fabrication. Electrochemical tests were conducted using a Palmsens4 workstation (Netherlands). CV and chronoamperometry (i-t) experiments were carried out in a 0.1 M PBS solution.

Electrochemical characterization of the electrode materials was performed using CV with $[Fe(CN)_6]^{3-/4-}$ as a redox probe. CV measurements were conducted in 5 mM $[Fe(CN)_6]^{3-/4-}$ solution containing 0.1 M KCl as the supporting electrolyte, over a range of scan rates (typically 10–200 mV/s). The ECSA of each electrode was calculated based on the Randles-Ševčík equation:

$$I_p = 2.72 \times 10^5 n^{3/2} A D^{1/2} C \nu^{1/2} \quad (1)$$

where I_p represents the redox peak current, n is the number of electrons transferred in the electrochemical reaction, A is the ECSA, D is the diffusion coefficient of the $[Fe(CN)_6]^{3-/4-}$ redox probe was taken as $D = 7.6 \times 10^{-6}$ cm^2 s^{-1}, C is the concentration of $[Fe(CN)_6]^{3-/4-}$, and ν is the scan rate. (Guo et al., 2019; Xu et al., 2022)

4.5. Application tests

An electrochemical sensor was fabricated using screen-printing technology, in which carbon served as both the working and counter electrodes, while silver/silver chloride functioned as the reference electrode. The working electrode was modified with MoCr-Pdene/C catalyst. The calibration curves of the electrochemical sensor at different concentrations (1 μM-2 mM) of TC in PBS solution were constructed. Artificial serum and artificial urine samples, free of TC, were employed as the testing matrices. Prior to analysis, each sample was diluted tenfold with PBS to minimize matrix interference. Three different concentrations of TC were then spiked into the diluted samples to assess the sensor's accuracy and applicability under simulated physiological conditions. For each concentration level, triplicate measurements were conducted using the MoCr-Pdene/C-modified sensor.

Beyond simulated clinical conditions, the MoCr-Pdene/C-modified sensor was further applied to evaluate TC degradation efficiency in a biological remediation system mediated by BSFL. The BSFL were reared in TC-contaminated organic feed (100 mg/kg) under controlled temperature (28 °C) and humidity (65 %) for 12 days. Abiotic control experiments were performed under the same conditions but without the addition of BSFL. After the degradation period, larval tissues and frass were collected separately, freeze-dried, and ground into fine powder. Each sample (0.5 g) was ultrasonically extracted with 10 mL of methanol-water (70:30, *v/v*) for 30 min, followed by centrifugation at 10,000 rpm for 10 min. The supernatant was filtered through a 0.22 μM membrane prior to electrochemical analysis.

During the measurements, 80 μL of solution was applied to the sensor, and current variations were monitored via the i-t tests. Each sample was assessed for 300 s, with the current at 200 s recorded as the response signal. To establish the calibration curve, the current range from 190 to 210 s was considered the error margin. This approach ensured robust evaluation of the sensor's accuracy, reproducibility, and anti-interference capability in complex biological matrices.

4.6. DFT calculation

DFT calculations were performed using the Vienna *ab initio* simulation package (Baroni and Testa, 1987; Kresse and Furthmuller, 1996a, 1996b; Kresse and Hafner, 1993, 1994; Kresse and Joubert, 1999). The projector augmented wave method was employed to describe the electron-ion interactions (Blochl, 1994), and the generalized gradient approximations with the Perdew-Burke-Ernzerhof functional was adopted for electron-electron exchange correlations (Perdew et al., 1997). The energy cutoff for the plane-wave basis set was set to 600 eV. A *k*-point mesh of 5 × 5 × 1 was set. The criteria for terminating electronic or ionic iterations were 1×10^{-4} eV, and the residual force on each atom was limited to less than 0.01 eV/Å. A vacuum space of about 15 Å was added to avoid interactions between periodic images. The D2 method was used to account for the van der Waals interaction (Bucko et al., 2010). The adsorption behaviors of TC molecule on the materials (Pene, Cr-Pdene, Mo-Pdene and MoCr-Pdene) surface ware then predicted using DFT calculations. The adsorption energies (E_{ad}) are defined as follows:

$$E_{ad} = E_{adsorbate} + E_{substrate} - E_{total} \quad (2)$$

where the E_{tot}, $E_{substrate}$ and $E_{adsorbate}$ are the total energy of molecule adsorbed on sensing materials, the energy of sensing materials and isolated molecule, respectively. A more positive E_{ad} value indicates stronger binding between the substrate and the adsorbate.

The free energy of species was calculated as follows:

$$G = E_{DFT} + E_{ZPE} - TS \quad (3)$$

where E_{DFT} is the reaction energy, which can be directly obtained from the DFT calculation. E_{ZPE} and S are the zero-point energy and entropy, respectively, which can be obtained by calculating the vibration frequencies. (Wang et al., 2021b) T is 298.15 K.

CRediT authorship contribution statement

Yi Wen: Conceptualization, Data curation, Formal analysis, Investigation, Methodology, Project administration, Resources, Software, Supervision, Validation, Visualization, Writing – original draft, Writing – review & editing. **Yinan Dong:** Data curation, Formal analysis, Methodology, Software, Writing – original draft. **Xuejie Shen:** Software, Writing – review & editing. **Xingyu Luo:** Resources. **Ziyi Wang:** Visualization. **Ruirui Guo:** Resources, Software. **Zhituo Geng:** Investigation. **Peng Li:** Resources. **Yongping Huang:** Funding acquisition. **Xinyu Zhu:** Investigation. **Jiatong Liu:** Investigation. **Wangyang Fu:** Conceptualization, Data curation, Project administration, Software, Supervision, Writing – review & editing. **Zehui Li:** Conceptualization, Data curation, Formal analysis, Funding acquisition, Investigation, Methodology, Project administration, Resources, Software, Supervision, Validation, Visualization, Writing – review & editing. **Xiaoyan Zhang:** Conceptualization, Data curation, Formal analysis, Funding acquisition, Investigation, Methodology, Project administration, Resources, Software, Supervision, Validation, Visualization, Writing – review & editing.

Declaration of competing interest

The authors declare that they have no known competing financial

interests or personal relationships that could have appeared to influence the work reported in this paper.

Acknowledgments

Y. Wen and Y. Dong contributed equally to this work. This work was supported by the National Natural Science Foundation of China (no. 52173007, 52073160 and 52470122), the Beijing Municipal Science and Technology Commission (no. Z221100005822003), the National Key Research and Development Program of China (no. 2024YFC3714000 and 2020YFF01014706), the Natural Science Foundation of Shanghai (no. 24ZR1433400), the Oceanic Interdisciplinary Program of Shanghai Jiao Tong University (no. SL2023MS013).

Appendix A. Supplementary data

Supplementary data to this article can be found online at https://doi.org/10.1016/j.bios.2026.118443.

Data availability

Data will be made available on request.

References

Ahmed, S.R., Sherazee, M., Das, P., Shalauddin, M., Akhter, S., Basirun, W.J., Srinivasan, S., Rajabzadeh, A.R., 2024. Biosens. Bioelectron. 246, 115857.
Baroni, Giannozzi, Testa, 1987. Phys. Rev. Lett. 58 (18), 1861–1864.
Blake, K.S., Xue, Y.-P., Gillespie, V.J., Fishbein, S.R.S., Tolia, N.H., Wencewicz, T.A., Dantas, G., 2025. Nat. Commun. 16 (1), 1452.
Blochl, P.E., 1994. Phys. Rev. B 50 (24), 17953–17979.
Bucko, T., Hafner, J., Lebegue, S., Angyan, J.G., 2010. J. Phys. Chem. A 114 (43), 11814–11824.
Cai, T., Han, Y., Wang, J., Li, W., Lu, X., Zhen, G., 2024. Water Res. 262, 122104.
Chen, K., Liu, S., Zhou, Y., Zhao, G., 2025. Environ. Sci. Technol. 59 (11), 5736–5746.
Chu, V.T., Tsitsiklis, A., Mick, E., Ambroggio, L., Kalantar, K.L., Glascock, A., Osborne, C. M., Wagner, B.D., Matthay, M.A., DeRisi, J.L., Calfee, C.S., Mourani, P.M., Langelier, C.R., 2024. Nat. Commun. 15 (1), 92.
Dang, X.P., Hu, C.G., Wei, Y.L., Chen, W.H., Hu, S.S., 2004. Electroanalysis 16 (23), 1949–1955.
Guo, H., Li, L., Chen, Y., Zhang, W., Shang, C., Cao, X., Li, M., Zhang, Q., Tan, H., Nie, Y., Gu, L., Guo, S., 2023. Adv. Mater. 35 (32), 302285.
Guo, H., Su, Y., Shen, Y., Long, Y., Li, W., 2019. J. Colloid Interface Sci. 536, 646–654.
Hammes-Schiffer, S., 2023. Nat. Comput. Sci. 3 (4), 291–300.
Heasley, B., 2011. Angew. Chem. Int. Ed. 50 (37), 8474–8477.
Khaled, O., Ryad, L., Eissa, F., 2024. Food Chem. 461, 140841.
Kresse, G., Furthmuller, J., 1996a. Comput. Mater. Sci. 6 (1), 15–50.
Kresse, G., Furthmuller, J., 1996b. Phys. Rev. B 54 (16), 11169–11186.
Kresse, G., Hafner, J., 1993. J. Non-Cryst. Solids 156, 956–960.
Kresse, G., Hafner, J., 1994. Phys. Rev. B 49 (20), 14251–14269.
Kresse, G., Joubert, D., 1999. Phys. Rev. B 59 (3), 1758–1775.
Li, H., Geng, W., Qi, Z., Ahmad, W., Chen, Q., 2023a. Biosens. Bioelectron. 226, 115122.
Li, J., Sun, X., Wang, M., Zhao, C., Yang, W., Tang, C., Bao, F., Shao, W., Xie, P., Xu, T., Liu, M., Li, H., Fu, J., 2023b. Adv. Membr. 3, 100077.
Li, Q., Cui, Y., Xiao, Y., Ni, Z., Dai, S., Chen, F., Guo, C., 2024a. Talanta 275, 126088.
Li, R., Liu, Y., Zhou, J., Cui, J., Chen, J., Li, Z., Chen, F., Liu, S., Mi, L., 2025. Biosens. Bioelectron. 280, 117430.
Li, Y., Peng, H., Li, H., Ma, Q., Zhang, X., Chen, Q., Li, J.-R., 2024b. Small 20 (48), 405436.
Liang, S., Lin, H., Yan, X., Huang, Q., 2018. Chem. Eng. J. 332, 628–636.
Liu, F., Hao, R., Zhao, Y., Zheng, C., Fallatah, A.M., Alhadhrami, A., Wang, Q., Wang, Y., Wang, F., Wang, Z., Liu, T.X., 2025a. Adv. Compos. Hybrid Mater. 8 (2), 191.
Liu, H., Li, T., Wu, Z., Xu, H., Li, H., Jing, R., Wang, Y., Liu, J., 2024a. Inorg. Chem. 64 (1), 123–132.
Liu, W., An, L., Li, P., Fu, Y., Zhang, X., Qu, D., Liu, Y., Hu, P., Wang, X., Jiang, N., Sun, Z., 2025b. Chem Catal. 5, 101357.
Liu, Z., Feng, L., Li, B., Lu, C., Sun, J., Giannakis, S., 2024b. J. Hazard. Mater. 480, 135854.
Liu, Z., Ge, X., Wang, Y., Niu, M., Yuan, W., Zhang, L.Y., 2023. Chem. Commun. 59 (77), 11588–11591.
Luo, M., Zhao, Z., Zhang, Y., Sun, Y., Xing, Y., Lv, F., Yang, Y., Zhang, X., Hwang, S., Qin, Y., Ma, J.-Y., Lin, F., Su, D., Lu, G., Guo, S., 2019. Nature 574 (7776), 81–85.
Ma, K., Liu, S., Teng, H., Miao, W., Zhou, X., Cui, X., Jiang, L., Zhou, X., 2025. Chem. Eng. J. 515, 163568.
Momeni, F., Khoshfetrat, S.M., Bagheri, H., Zarei, K., 2024. Biosens. Bioelectron. 250, 116078.
Naikoo, G.A., Arshad, F., Hassan, I.U., Omar, F.B., Tambuwala, M.M., Mustaqeem, M., Saleh, T.A., 2023. TrAC, Trends Anal. Chem. 162, 117042.
Nekoueian, K., Kontturi, K.S., Meinander, K., Quliyeva, U., Kousar, A., Durairaj, V., Tammelin, T., Laurila, T., 2024. Electrochim. Acta 500, 144639.
Perdew, J.P., Burke, K., Ernzerhof, M., 1997. Phys. Rev. Lett. 78 (7), 1396-1396.
Prabhu, P., Do, V.-H., Yoshida, T., Zhou, Y., Ariga-Miwa, H., Kaneko, T., Uruga, T., Iwasawa, Y., Lee, J.-M., 2024. ACS Nano 18 (14), 9942–9957.
Qiu, Y., Fan, J., Wu, J., Lu, W., Wang, S., Wang, D., Ge, X., Zhao, X., Zhang, W., Zheng, W., Cui, X., 2023. Nano Lett. 23 (20), 9555–9562.
Rong, M., Huang, Y., Lin, C., Lai, L., Wu, Y., Niu, L., 2024. TrAC, Trends Anal. Chem. 178, 117839.
Si, Y., Huang, Y., Qin, C., Huang, Y., Guo, X., Gao, X., Yao, S., Cheng, Y., 2024. ACS Catal. 14 (22), 17180–17190.
Song, X., Xiong, W., He, H., Si, D., Lu, L., Peng, Y., Jiang, Q., Wang, Y., Zheng, Y., Nan, Z.-A., Wang, Q., Chen, M., Cao, R., Fan, F.R., 2024. Nano Energy 122, 109275.
Sun, J., Dai, W.Q., Guo, Q., Gao, Y.R., Chen, J.Y., Chen, J.L., Mao, G.Z., Sun, H.Y., Peng, Y.K., 2025. Biosens. Bioelectron. 277, 117303.
Wang, L., Wang, A., Wan, X., Yu, W., Wang, X., Li, Z., Li, L., Guo, Y., Zhang, Z., Zhao, Y., 2025a. J. Mater. Chem. A 13 (24), 18358–18366.
Wang, M., Wang, Y., Li, Y., Wang, C., Kuang, S., Ren, P., Xie, B., 2023. Chem. Eng. J. 464, 142558.
Wang, M., Ye, C., Yang, Y., Mukasa, D., Wang, C., Xu, C., Min, J., Solomon, S.A., Tu, J., Shen, G., Tang, S., Hsiai, T.K., Li, Z., McCune, J.S., Gao, W., 2025b. Nat. Mater. 24 (4), 589–598.
Wang, Q., Xue, Q., Chen, T., Li, J., Liu, Y., Shan, X., Liu, F., Jia, J., 2021a. Chin. Chem. Lett. 32 (2), 609–619.
Wang, V., Xu, N., Liu, J.C., Tang, G., Geng, W.T., 2021b. Comput. Phys. Commun. 267, 108033.
Wei, X., Yin, M., Zhang, L., Sun, Y., Luo, Y., Xu, D., 2024. Spectrochim. Acta 304, 123361.
Wei, Z., Zhao, Z., Qiu, C., Huang, S., Yao, Z., Wang, M., Chen, Y., Lin, Y., Zhong, X., Li, X., Wang, J., 2023. Nat. Commun. 14 (1), 661.
Wu, J., Liu, H., Chen, W., Ma, B., Ju, H., 2023. Nat. Rev. Bioeng. 1 (5), 346–360.
Xie, L., Wang, J., Wang, K., He, Z., Liang, J., Lin, Z., Wang, T., Cao, R., Yang, F., Cai, Z., Huang, Y., Li, Q., 2024. Angew. Chem. Int. Ed. 63 (44), e202407658.
Xie, S., Fu, J., Huang, Q., Yang, W., Yu, A., Yan, Y., Li, Z., Peng, P., Yin, Y., Wang, H., Echegoyen, L., Li, F.-F., 2025. Angew. Chem. Int. Ed., e202506044
Xu, H., Zhang, D., Weng, X., Wang, D., Cai, D., 2022. Microchim. Acta 189 (5), 201.
Xu, H., Zhou, C., Li, X., 2024. Chem. Eng. J. 501, 157537.
Xu, H.Y., Chen, Q., Meng, X.Z., Yan, C., Yao, B.B., Chen, Z.R., Wang, Z.Z., Chen, W., 2025a. Biosens. Bioelectron. 277, 117284.
Xu, X., Huang, Y.P., Luo, X.Y., 2025b. Natl. Sci. Rev. 12 (3) nwaf043.
Xuan, C., Xu, Q., Han, L., Hou, B., 2023. Chem. Eng. J. 464, 142620.
Yang, L., Wang, X., Zhang, F., Yu, L., Bai, B., Zhang, J., Zhang, B., Tian, Y., Qin, S., Yang, Y., 2024a. Food Chem. 430, 136904.
Yang, R., Sun, K., Mao, Q., Wang, W., Deng, K., Wang, J., Yu, H., Wang, L., Wang, H., 2024b. Small 20 (52), 407446.
Zhan, F., Zhao, Y., Dai, X., Zeng, J., Wang, Q., 2024. Microchem. J. 196, 109512.
Zhang, J., Lv, F., Li, Z., Jiang, G., Tan, M., Yuan, M., Zhang, Q., Cao, Y., Zheng, H., Zhang, L., Tang, C., Fu, W., Liu, C., Liu, K., Gu, L., Jiang, J., Zhang, G., Guo, S., 2022. Adv. Mater. 34 (2), 2105276.
Zhang, W., Zhang, W., Tan, J., Pan, D., Tang, Y., Gao, Q., 2023. J. Mater. Chem. A 11 (14), 7505–7512.
Zhao, J., Wang, M., Peng, Y., Ni, J., Hu, S., Zeng, J., Chen, Q., 2023. Angew. Chem. Int. Ed. 62 (30), e202304424.
Zhao, W., Zhao, N., 2023. J. Food Meas. Char. 17 (3), 2623–2629.